

## Nonlinear gyrokinetic turbulence simulations of $E \times B$ shear quenching of transport

Cite as: Phys. Plasmas **12**, 062302 (2005); <https://doi.org/10.1063/1.1920327>

Submitted: 08 February 2005 • Accepted: 31 March 2005 • Published Online: 26 May 2005

J. E. Kinsey, R. E. Waltz and J. Candy



View Online



Export Citation

### ARTICLES YOU MAY BE INTERESTED IN

[Comparisons and physics basis of tokamak transport models and turbulence simulations](#)

Physics of Plasmas **7**, 969 (2000); <https://doi.org/10.1063/1.873896>

[Electron temperature gradient driven turbulence](#)

Physics of Plasmas **7**, 1904 (2000); <https://doi.org/10.1063/1.874014>

[Effects of  \$E \times B\$  velocity shear and magnetic shear on turbulence and transport in magnetic confinement devices](#)

Physics of Plasmas **4**, 1499 (1997); <https://doi.org/10.1063/1.872367>



**Physics of Plasmas   Physics of Fluids**  
**Special Topic: Turbulence in Plasmas and Fluids**  
 Submit Today!

# Nonlinear gyrokinetic turbulence simulations of $E \times B$ shear quenching of transport

J. E. Kinsey

*Lehigh University, Bethlehem, Pennsylvania 18015*

R. E. Waltz and J. Candy

*General Atomics, P.O. Box 85608, San Diego, California 92186*

(Received 8 February 2005; accepted 31 March 2005; published online 26 May 2005)

The effects of  $E \times B$  velocity shear have been investigated in nonlinear gyrokinetic turbulence simulations with and without kinetic electrons. The impact of  $E \times B$  shear stabilization in electrostatic flux-tube simulations is well modeled by a simple quench rule with the turbulent diffusivity scaling like  $1 - \alpha_E \gamma_E / \gamma_{\max}$ , where  $\gamma_E$  is the  $E \times B$  shear rate,  $\gamma_{\max}$  is maximum linear growth rate without  $E \times B$  shear, and  $\alpha_E$  is a multiplier. The quench rule was originally deduced from adiabatic electron ion temperature gradient (ITG) simulations where it was found that  $\alpha_E \approx 1$ . The results presented in this paper show that the quench rule also applies in the presence of kinetic electrons for long-wavelength transport down to the ion gyroradius scale. Without parallel velocity shear, the electron and ion transport is quenched near  $\gamma_E / \gamma_{\max} \approx 2$  ( $\alpha_E \approx 1/2$ ). When the destabilizing effect of parallel velocity shear is included in the simulations, consistent with purely toroidal rotation, the transport may not be completely quenched by any level of  $E \times B$  shear because the Kelvin–Helmholtz drive increases  $\gamma_{\max}$  faster than  $\gamma_E$  increases. Both ITG turbulence with added trapped electron drive and electron-directed and curvature-driven trapped electron mode turbulence are considered. © 2005 American Institute of Physics. [DOI: 10.1063/1.1920327]

## I. INTRODUCTION

The stabilization of long-wavelength drift-wave turbulence by  $E \times B$  rotational shear has long been established as a key mechanism leading to the formation of core and edge transport barriers in tokamaks. Early works described  $E \times B$  shear stabilization within the context of a suppression mechanism.<sup>1–3</sup> In later works by Waltz *et al.*,<sup>4–6</sup> it was found that the transport can be quenched by  $E \times B$  shear based on gyrofluid flux-tube simulations in shifted circle geometry assuming adiabatic electrons. These ion temperature gradient (ITG) simulations lead to the development of a quench rule whereby the turbulent transport is eliminated when the critical  $E \times B$  shear rate  $\gamma_E = (r/q) \partial(qv_{E \times B}/r) / \partial r$  exceeds the maximum linear ballooning mode growth rate  $\gamma_{\max}$  computed in the absence of  $E \times B$  shear. This quench rule was first incorporated in the eigenvalue-based gyrofluid GLF23 transport model<sup>7,8</sup> and later in the formula-based gyrofluid Institute for Fusion Studies–Princeton Plasma Physics Laboratory (IFS/PPPL) model<sup>9</sup> and other models as a factor  $[1 - \alpha_E \gamma_E / \gamma_{\max(0)}]$  multiplying the diffusivities. The ITG gyrofluid simulations suggested  $\alpha_E \approx 1$ . However, in recent circular ITG gyrokinetic simulations it was found that  $\alpha_E \approx 0.6$ .<sup>10</sup> These simulations confirm the results by Dimits *et al.*<sup>11</sup> suggesting that stronger  $E \times B$  shear rates are needed to quench transport in gyrokinetic simulations than in gyrofluid simulations. Real geometry ITG simulations including elongation suggested that  $\alpha_E \approx 0.6$ .<sup>12</sup> In any case, the quench rule has proven to be successful in reproducing observed core barriers in transport simulations.<sup>8,13</sup> In addition, experimentally derived values of the  $E \times B$  shear rate has been found to be in the range of ITG and trapped electron mode (TEM)

growth rates,<sup>14–19</sup> thus lending support to the  $E \times B$  shear paradigm of transport barrier formation.

Previous simulations have focused on the effect of  $E \times B$  shear on unstable ITG drift-wave modes rotating in the ion direction. It has been unclear how ITG/trapped electron (TE) mode transport with maximum linear growth rates at somewhat shorter wavelengths (i.e.,  $k_{\theta} \rho_s \geq 0.5$ ) responds to  $E \times B$  shear stabilization. Linear sheared slab calculations indicate that a larger  $E \times B$  shear is required to stabilize TE modes.<sup>20</sup> Thus, we are motivated to explore the validity of the quench rule in ITG/TE simulations with kinetic electrons, quantify any variance in  $\alpha_E$ , and assess how low to mid- $k_{\theta} \rho_s$  TEM turbulence responds to  $E \times B$  shear. It is generally believed that electron temperature gradient (ETG) modes are insensitive to  $E \times B$  shear.<sup>21,22</sup> We make no attempt here to describe the transport with a mode spectrum that ranges from long-wavelength ITG/TE mode to short-wavelength ETG modes with nonadiabatic ions and electrons.

In this work, we report on results of nonlinear gyrokinetic simulations around several reference parameters and focus on the effect of equilibrium  $E \times B$  rotational shear on the turbulent transport due to ITG/TE modes in toroidal geometry. We compare cases where the modes are rotating in the ion direction with cases where the modes are primarily rotating in the electron direction. The simulations were performed using the GYRO gyrokinetic continuum code.<sup>23</sup> GYRO is a physically comprehensive continuum global gyrokinetic code. Our goal is to elucidate the effect of  $E \times B$  shear on toroidal drift-wave turbulence including the physics of kinetic electrons. We compare these results to those from adiabatic electron simulations and examine any variance in the quench point of the turbulence. These gyrokinetic simu-

lations also serve as important benchmarks for other turbulence codes and for transport model testing and construction.

The paper is organized as follows. First, we revisit nonlinear ITG simulations with adiabatic electrons for a reference set of parameters hereby referred to as the standard (STD) case. Shown are the gyrokinetic results for the standard case accompanied by a scan in equilibrium  $E \times B$  shear. Next, a comparison is made between  $E \times B$  shear scans at various values of the global magnetic shear. Simulation results are also shown for an adiabatic electron  $E \times B$  shear scan including the destabilizing effects of parallel velocity shear. We then discuss simulations of the standard case including kinetic electrons as well as several cases where the unstable ballooning modes within the spectrum are primarily in the electron direction. Finally, some concluding remarks are given.

## II. NONLINEAR GYROKINETIC SIMULATIONS WITH ADIABATIC ELECTRONS

In this section we present nonlinear ITG simulation results using the GYRO gyrokinetic code.<sup>23</sup> GYRO is a physically comprehensive global code which solves the nonlinear gyrokinetic equations for both ions and electrons. GYRO uses a Eulerian discretization scheme (also called a continuum scheme) in contrast to the more popular Lagrangian, or particle-in-cell (PIC), method. The first-order differential operators which describe parallel and drift motion are discretized using time-explicit high-order upwind schemes. One exception is the stiff electron parallel motion, which is treated implicitly. Accuracy of the collisionless time advance is fully second-order (via an implicit-explicit Runge–Kutta method), including nonlinear and implicit terms.

Although GYRO has real geometry capabilities, all the simulations reported in this paper assume a shifted circle ( $\hat{s}-\alpha$ ) geometry<sup>24</sup> for a radial annulus. While GYRO can include electromagnetic effects, radial profile variations, impurities, and collisions, we do not include them in our simulations. We use a 128-point velocity space discretization (8 pitch angles, 8 energies, and 2 signs of velocity). With the exception of a few cases, 16 toroidal mode numbers were used. We believe the simulations are run long enough to achieve statistically steady-state levels with adequate time stepping and box sizes. We have also performed convergence tests which establish the adequacy of the time step, box size, etc.

### A. The standard case

We first consider the standard case with adiabatic electrons, no equilibrium  $E \times B$  shear and no parallel velocity shear. With adiabatic electrons there is no net particle transport. Also, there is no electron heat transport since electron temperature gradient fluctuations are not included. The parameters for the STD case from Ref. 8 are  $k_\theta \rho_s = (nq/r)\rho_s = 0.3$ ,  $R/a = 3.0$ ,  $r/a = 0.5$ ,  $q = 2$ ,  $\hat{s} = 1.0$ ,  $\beta = 0$ ,  $\alpha = 0$ ,  $a/L_n = 1.0$ ,  $a/L_T = 3.0$ ,  $(a/c_s)\nu_{ei} = 0.0$ ,  $T_i/T_e = 1.0$ , and  $(a/c_s)\gamma_p = 0.0$ . Here,  $\rho_s$  is the Larmor radius equal to  $c_s/\Omega_{ci}$  where  $c_s = \sqrt{T_e/m_i}$  is the sound speed and  $\Omega_{ci}$  is the ion cyclotron frequency. Also, we have the logarithmic gradients where,

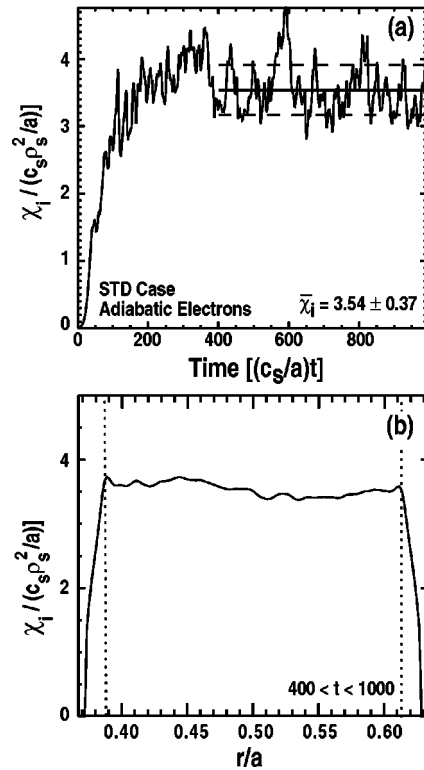


FIG. 1. Nonlinear simulation of the standard case with adiabatic electrons using the GYRO gyrokinetic code. (a) Time trace of turbulent ion heat diffusivity. (b) Time-averaged radial ion temperature profile. The vertical dotted lines indicate the location of the benign boundary layers.

for example,  $1/L_T = d \ln T / dr$  with  $r = (R_{out} + R_{in})/2$  as the average midplane minor radius, the magnetic shear  $\hat{s} = (r/q)\partial q / \partial r$ , the plasma beta  $\beta$ , the magnetohydrodynamics (MHD) alpha parameter  $\alpha = -q^2 R d\beta / dr$ , the electron–ion collision frequency  $\nu_{ei}$ , and the parallel velocity shear rate  $\gamma_p = (\partial v_{||} / \partial r)$ . In these GYRO simulations, we included 16 modes with a toroidal spacing of  $\Delta n = 5$  at  $\rho_s/a = 0.0025$ , a maximum  $k_\theta \rho_s = 0.75$ ,  $\sqrt{m_i/m_e} = 60$ , and a box size of  $[L_x/\rho_s, L_y/\rho_s] = [107, 126]$ . Using 120 radial grid points proved sufficient for the adiabatic electron simulations. To eliminate any nonphysical boundary effects associated with the introduction of  $E \times B$  Doppler shear, we use fixed (non-periodic) radial zero-value benign boundary layers<sup>10</sup> for all the nonlinear simulations shown in this paper. Previously, it was shown that simulations with these fixed boundary conditions recover the simulation results (i.e., diffusivity) with cyclic boundary conditions across an annulus (without profile variation and Doppler rotation).<sup>10</sup> Figure 1 shows the time evolution [Fig. 1(a)] and time-averaged radial profile [Fig. 1(b)] of the turbulent ion heat diffusivity without  $E \times B$  shear. The dashed lines in Fig. 1(b) indicate the location of the benign boundary layers. Here, the time averaging was taken over  $400 \leq (c_s/a)\Delta t \leq 1000$  to yield an ion heat diffusivity of  $\bar{\chi}_i / (c_s \rho_s^2 / a) = 3.54 \pm 0.37$ . The rms deviation relative to the average is a measure of the intermittency in the box-averaged diffusivity. The corresponding maximum linear growth rate and frequency is  $[\gamma_{max}, \omega] = [0.13, -0.31](c_s/a)$

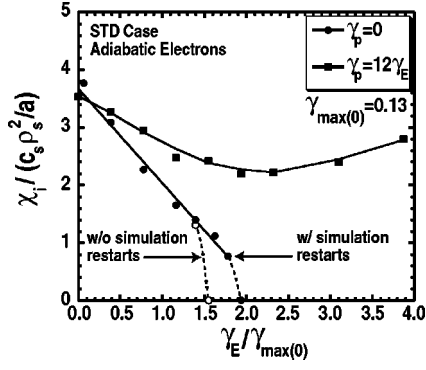


FIG. 2. Ion heat diffusivity vs  $\gamma_E/\gamma_{\max(0)}$  with (squares) and without (circles) the destabilizing effect of parallel velocity shear  $\gamma_p$ . The points indicate the GYRO results and the lines are curve fits.

at  $k_{\theta}\rho_s=0.33$ . The peak in the ITG transport is near  $k_{\theta}\rho_s=0.15$  and is always downshifted from the location of maximum growth rate.

### B. Equilibrium $E \times B$ shear scan

Here, we proceed with the standard case with adiabatic electrons and show the results of scans in equilibrium  $E \times B$  rotational shear. Previous published results described the effect of  $E \times B$  shear stabilization of ITG transport in nonlinear three-dimensional (3D) gyrofluid flux-tube simulations of a cyclic annulus.<sup>6</sup> For the standard case, it was found that the quench point at  $\gamma_E/\gamma_{\max}=1$  showed fairly good invariance for various values of magnetic shear from  $\hat{s}=0.25$  to 2.0. Here,  $\gamma_{\max}$  is the maximum linear growth rate computed in the absence of  $E \times B$  shear. We find that the corresponding GYRO ITG gyrokinetic simulations exhibit an adiabatic electron quench point that is approximately  $\gamma_E/\gamma_{\max(0)}=2$ . This is somewhat higher than what was found in previous gyrokinetic simulations where the quench appeared to be at  $\gamma_E/\gamma_{\max}=1.7$ .<sup>10</sup> Figure 2 shows the ion diffusivity versus  $\gamma_E/\gamma_{\max(0)}$  with (squares) and without (circles) the destabilizing effect of parallel velocity shear  $\gamma_p$ . The points indicate the GYRO results and the lines are curve fits. The results are listed in Tables II and III. Here,  $\gamma_{\max(0)}$  is the maximum linear growth rate computed with  $\gamma_p=0$ . When the destabilizing effect of parallel velocity shear is included in the simulations, consistent with purely toroidal rotation, the ITG transport is not quenched by any level of  $E \times B$  shear be-

TABLE I. Maximum linear growth rates and frequencies.

	$\gamma_{\max(0)}$	$\omega$	$k_{\theta}\rho_s$
Adiabatic electrons case			
STD ( $\hat{s}=-0.5$ )	0.12	-0.29	0.45
STD ( $\hat{s}=1.0$ )	0.13	-0.31	0.33
STD ( $\hat{s}=1.5$ )	0.08	-0.34	0.36
Kinetic electrons case			
STD ( $\hat{s}=1.0$ )	0.24	-0.33	0.31
TEM1	0.28	-0.01	0.29
TEM2	0.43	0.03	0.51

TABLE II. Adiabatic electron results for the ion heat diffusivity  $\bar{\chi}_i/\chi_{GB}$  for the standard case with  $E \times B$  shear and no parallel velocity shear ( $\gamma_p=0$ ).

$(a/c_s)\gamma_E$	Ion heat diffusivity $\bar{\chi}_i/\chi_{GB}$
$\gamma_E$ applied at $t=0$	
0.0	$3.54 \pm 0.37$
0.05	$3.09 \pm 0.37$
0.10	$2.27 \pm 0.15$
0.15	$1.65 \pm 0.10$
0.18	$1.31 \pm 0.08$
0.20	0
$\gamma_E$ applied after restart	
0.18	$1.40 \pm 0.09$
0.21	$1.12 \pm 0.07$
0.23	$0.77 \pm 0.06$
0.25	0

cause the Kelvin-Helmholtz drive increases  $\gamma_{\max}$  faster than  $\gamma_E$  increases.<sup>4</sup> In fact, above  $\gamma_E/\gamma_{\max(0)} \approx 2$ , the transport then begins to rise with increasing  $\gamma_E$  (and  $\gamma_p$ ). Here, the parallel velocity shear rate is computed as  $\gamma_p=(Rq/r)\gamma_E=12\gamma_E$  with  $R/a=3$ ,  $r/a=0.5$ , and  $q=2$  assuming purely toroidal rotation. For example, at  $\gamma_E/\gamma_{\max(0)}=3.1$  we have  $\gamma_E=0.40$  and  $\gamma_p=4.8$ . Here,  $\gamma_{\max(0)}=0.13$ . With  $\gamma_p=4.8$ ,  $\gamma_{\max}$  is 0.29, yielding a ratio of  $\gamma_E/\gamma_{\max}=1.46$ , which is less than 2 where the quench point should be found. So, when  $\gamma_E/\gamma_{\max}$  computed with  $\gamma_p$  lags behind the quench value of  $\gamma_E/\gamma_{\max(0)}$ , the transport will not be quenched by any  $\gamma_E$ . We note that inside the barrier region of ITB discharges, the safety factor is often larger than 2 and  $r/a$  is less than 0.5, making  $Rq/r$  larger than 12. Parallel velocity shear may explain why turbulence is not completely quenched experimentally in core barriers, but appears to be only suppressed. In edge barriers (i.e.,  $H$ -mode pedestal region),  $\gamma_p$  is not large compared with  $\gamma_E$  because the diamagnetic rotation tends to dominate over the toroidal rotation contribution to  $\gamma_E$ .

Interestingly, we also find that two different turbulent steady states can be found near the quench point ( $\gamma_p=0$ ) depending upon how the  $E \times B$  shear is applied. The quench point occurs at a higher value of  $\gamma_E/\gamma_{\max}$  if the  $E \times B$  shear is

TABLE III. Adiabatic electron results with  $E \times B$  shear and with parallel velocity shear ( $\gamma_p=12\gamma_E$ ) for the standard case, and ion heat and toroidal momentum  $\bar{\chi}_{i,\phi}/\chi_{GB}$  diffusivities with  $\gamma_E$  applied at  $t=0$ .

$(a/c_s)\gamma_E$	$(a/c_s)\gamma_p$	$\bar{\chi}_i$	$\bar{\chi}_{\phi}$
0.0	0.0	$3.54 \pm 0.37$	$0.0 \pm 0.0$
0.05	0.6	$3.27 \pm 0.30$	$1.51 \pm 0.45$
0.10	1.2	$2.95 \pm 0.28$	$1.75 \pm 0.18$
0.15	1.8	$2.48 \pm 0.17$	$1.61 \pm 0.15$
0.20	2.4	$2.42 \pm 0.18$	$1.59 \pm 0.11$
0.25	3.0	$2.20 \pm 0.12$	$1.53 \pm 0.08$
0.30	3.6	$2.22 \pm 0.14$	$1.58 \pm 0.09$
0.40	4.8	$2.40 \pm 0.14$	$1.76 \pm 0.10$
0.50	6.0	$2.80 \pm 0.14$	$2.08 \pm 0.13$



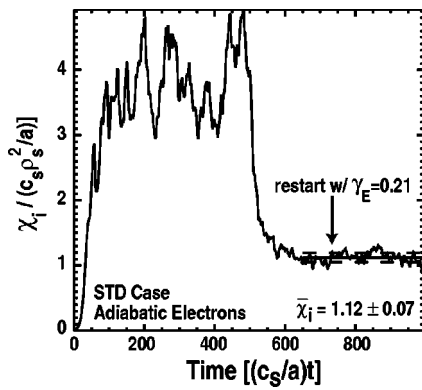


FIG. 3. Time evolution of the ion heat diffusivity for the standard case with adiabatic electrons initiated with  $\gamma_E=0$  then restarted at  $(c_s/a)t=500$  with  $\gamma_E$  reset to 0.21 [ $\gamma_E/\gamma_{\max(0)}=1.63$ ].

applied restarting from a  $\gamma_E=0$  simulation rather than starting a new simulation with  $\gamma_E>0$ . A scan in  $\gamma_E$  of the standard case with the  $E \times B$  shear applied from the beginning the simulation show that the ITG transport is quenched close to  $\gamma_E/\gamma_{\max}=1.55$  with a sharp drop in the diffusivity near the quench point (dashed line with hollow circles). In the  $\gamma_E/\gamma_{\max}=1.55$  ( $\gamma_E=0.20$ ) simulation, the maximum amplitude of the  $n=0$  zonal flow potential exceeds the maximum amplitude of the low- $k$  ITG mode potentials and the turbulence levels never rise above zero. Just above the quench point, we find that very long simulations are needed in order for the turbulence levels to saturate. For example, in the case with  $\gamma_E/\gamma_{\max}=1.4$ , the turbulence levels did not noticeably rise until after  $(c_s/a)t=1100$ .

For simulations which are restarted from a reference simulation with  $\gamma_E=0$ , the quench point is 35% higher than what is found from the simulations with an initial  $\gamma_E$ . In particular, we find that the quench point occurs at a value of  $\gamma_E/\gamma_{\max}=1.95$  (the solid circles). We note that a strictly linear fit to the solid circles would yield a quench point closer to 2.1. Figure 3 shows the time evolution of the ion diffusivity for the restarted case with  $\gamma_E/\gamma_{\max(0)}=1.63$ . Here, the simulation was restarted from  $\gamma_E=0$  conditions at a time of  $(c_s/a)t=500$  with  $\gamma_E$  reset to 0.21. After  $(c_s/a)t=500$ , the ITG transport is strongly suppressed, resulting in a saturated

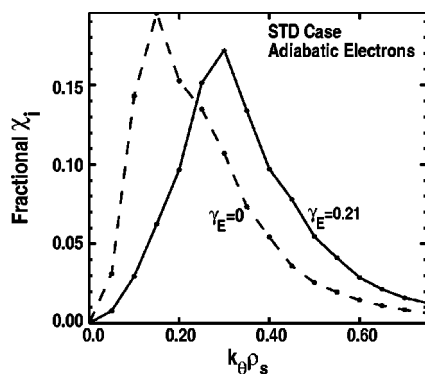


FIG. 4. Normalized fractional ion heat diffusivity vs  $k_\theta \rho_s$  time averaged for the case  $\gamma_E=0$  (dashed line) and for the restarted case with  $\gamma_E=0.21$  (solid line). Both are for the standard parameters with adiabatic electrons.

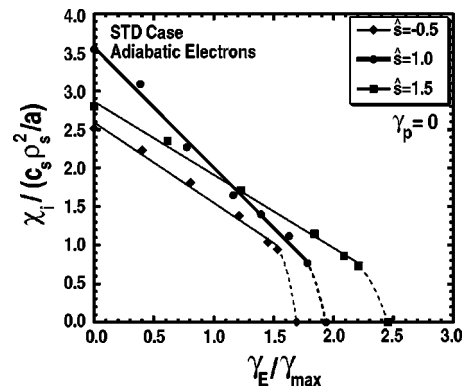


FIG. 5. Ion heat diffusivity vs  $\gamma_E/\gamma_{\max(0)}$  for the standard case with adiabatic electrons and  $\gamma_p=0$  for magnetic shear values of  $-0.5$  (diamonds),  $1.0$  (circles), and  $1.5$  (squares). The solid lines are linear fits to the GYRO points and the dashed lines are smooth fits near the ITG quench point.

time-averaged diffusivity of  $\bar{\chi}_i=1.12\pm0.07/\chi_{GB}$ . Here,  $\chi_{GB}=(c_s \rho_s^2/a)$ . Figure 4 shows how the spectrum has shifted to higher wave number  $k_\theta \rho_s$  as the critical  $\gamma_E$  is approached (area under the curve equals unity). This suggests that  $E \times B$  shear has the strongest effect on the long-wavelength modes where  $\gamma_E > 2[\gamma_k/\gamma_{\max(0)}]$ .<sup>6</sup>

There is approximately a 25% variation in the quench point for global shear values of  $\hat{s}=-0.5$ ,  $1.0$ , and  $1.5$  (Fig. 5). The GYRO results are listed in Table IV. Here,  $\gamma_{\max(0)}$  is  $0.12$ ,  $0.13$ , and  $0.08$ , respectively (Table I). The case with  $\hat{s}=1.5$  has the highest quench point at  $\gamma_E/\gamma_{\max(0)}=2.45$ . The solid lines indicate linear fits to the GYRO points ignoring the  $\chi=0$  point. The dotted line corresponds to a smooth fit to the last three GYRO points including the quench point. Note the rapid drop in  $\chi$  with a sharp increase in the slope as the quench point is approached. We did not observe this rapid drop from turbulence levels near  $\bar{\chi}/\chi_{GB}=0.75$  in similar scans with kinetic electrons as shown in Sec. III [where a

TABLE IV. Adiabatic electron results for the ion heat diffusivity  $\bar{\chi}_i/\chi_{GB}$  for the standard case at magnetic shear values of  $\hat{s}=-0.5$  and  $1.5$  with  $\gamma_E=0$ .

$(a/c_s)\gamma_E$	Ion heat diffusivity, $\bar{\chi}_i/\chi_{GB}$
$\hat{s}=-0.5$	
0.0	$2.51\pm0.21$
0.05	$2.23\pm0.16$
0.10	$1.81\pm0.14$
0.15	$1.38\pm0.12$
0.18	$1.04\pm0.09$
0.19	$0.95\pm0.07$
0.21	0
$\hat{s}=1.5$	
0.0	$2.80\pm0.22$
0.05	$2.35\pm0.17$
0.10	$1.71\pm0.12$
0.15	$1.15\pm0.07$
0.17	$0.86\pm0.07$
0.18	$0.73\pm0.07$
0.20	0

TABLE V. Kinetic electron results for  $E \times B$  shear scans around the standard case with and without parallel velocity shear ( $\gamma_p = 12\gamma_E$  with  $\gamma_E$  restarts), and ion and electron heat diffusivities  $\bar{\chi}_{i,e}/\chi_{GB}$ .

$(a/c_s)\gamma_E$	$(a/c_s)\gamma_p$	$\bar{\chi}_i/\chi_{GB}$	$\bar{\chi}_e/\chi_{GB}$
$\gamma_p = 0$			
0.0	0.0	$10.7 \pm 2.6$	$3.2 \pm 0.6$
0.05	0.0	$8.5 \pm 1.5$	$2.7 \pm 0.4$
0.10	0.0	$6.0 \pm 0.7$	$2.0 \pm 0.2$
0.15	0.0	$4.8 \pm 0.5$	$1.7 \pm 0.2$
0.20	0.0	$4.0 \pm 0.4$	$1.4 \pm 0.1$
0.30	0.0	$2.3 \pm 0.2$	$0.8 \pm 0.06$
0.40	0.0	$1.1 \pm 0.07$	$0.4 \pm 0.03$
0.50	0.0	$0.5 \pm 0.04$	$0.3 \pm 0.02$
$\gamma_p = 12\gamma_E$			
0.05	0.6	$8.8 \pm 1.1$	$2.5 \pm 0.3$
0.10	1.2	$7.3 \pm 0.9$	$2.2 \pm 0.2$
0.20	2.4	$5.7 \pm 0.7$	$1.7 \pm 0.2$
0.30	3.6	$5.1 \pm 0.4$	$1.6 \pm 0.2$
0.40	4.8	$4.7 \pm 0.4$	$1.6 \pm 0.1$
0.50	6.0	$4.6 \pm 0.4$	$1.7 \pm 0.2$

much longer tail in the transport versus  $\gamma_E/\gamma_{\max(0)}$  is seen with a drop to the quench point from a much lower  $\chi_i$ .

It is also evident from this scan that the  $\hat{s} = -0.5$  and  $\hat{s} = 1.5$  cases show a weaker dependence on  $\gamma_E$  than the  $\hat{s} = 1$  case. Since the peak in the growth rates tends to occur at  $\hat{s} - \alpha = 0.5$ , it is possible that the  $E \times B$  shear dependence weakens as the magnetic shear moves away from the peak. This may be sensible since the peak in the transport shifts to higher wave numbers as  $\hat{s}$  shifts away from  $\hat{s} - \alpha = 0.5$ . However, more scans in  $\gamma_E$  at other values of  $\hat{s}$  are needed to elucidate the dependence on  $\hat{s}$  further.

### III. NONLINEAR GYROKINETIC SIMULATIONS WITH KINETIC ELECTRONS

While numerous simulations have been performed with adiabatic electrons to explore the effects of global shear  $\hat{s}$  and equilibrium  $E \times B$  shear on transport, little is known about the behavior of drift-wave transport when kinetic elec-

TABLE VI. Kinetic electron results for  $E \times B$  shear scans around the TEM1 case without parallel velocity shear, and ion and electron heat diffusivities  $\bar{\chi}_{i,e}/\chi_{GB}$ . Standard parameters with  $a/L_n = 2$  and  $a/L_T = 2$ .

$(a/c_s)\gamma_E$	$\bar{\chi}_i/\chi_{GB}$	$\bar{\chi}_e/\chi_{GB}$
0.0	$11.0 \pm 2.2$	$11.3 \pm 2.2$
0.05	$10.2 \pm 1.6$	$10.4 \pm 1.6$
0.10	$8.9 \pm 1.7$	$9.1 \pm 1.7$
0.20	$6.7 \pm 0.9$	$7.0 \pm 0.9$
0.30	$5.8 \pm 0.6$	$6.1 \pm 0.6$
0.40	$4.6 \pm 0.4$	$4.8 \pm 0.5$
0.50	$2.6 \pm 0.2$	$2.8 \pm 0.2$
0.60	$1.2 \pm 0.09$	$1.2 \pm 0.09$
0.70	$0.6 \pm 0.04$	$0.6 \pm 0.03$
0.90	$0.3 \pm 0.02$	$0.5 \pm 0.02$

TABLE VII. Kinetic electron results for  $E \times B$  shear scans around the TEM2 case without parallel velocity shear, and ion and electron heat diffusivities  $\bar{\chi}_{i,e}/\chi_{GB}$ . Standard parameters with  $a/L_n = 3$  and  $a/L_T = 1$ .

$(a/c_s)\gamma_E$	$\bar{\chi}_i/\chi_{GB}$	$\bar{\chi}_e/\chi_{GB}$
0.0	$20.5 \pm 4.8$	$23.9 \pm 5.9$
0.10	$19.7 \pm 4.4$	$22.9 \pm 5.4$
0.20	$16.3 \pm 2.7$	$18.9 \pm 3.2$
0.30	$14.6 \pm 2.8$	$16.9 \pm 3.4$
0.40	$12.9 \pm 1.8$	$15.0 \pm 2.2$
0.50	$10.1 \pm 1.1$	$11.6 \pm 1.3$
0.60	$7.9 \pm 0.9$	$9.1 \pm 1.0$

trons are included. In this section, we report the results of the GYRO simulations with kinetic electrons for the standard case and for the two cases where the trapped electron drive tends to drive the turbulence in the electron direction. The impact of  $E \times B$  shear is again studied with and without parallel velocity shear.

#### A. The standard case

We again consider the standard case but now include kinetic electron physics in the simulations. Trapped electrons increase the drive for ITG modes and can give rise to TEMs driven primarily by the toroidal trapped electron precession. In the GYRO simulations, we again restrict ourselves to  $\hat{s} - \alpha$  geometry for an annulus with a domain size of  $[L_x/\rho_s, L_y/\rho_s] = [107, 126]$ . For most of the kinetic electron simulations we use a time step of  $(c_s/a)\Delta t = 0.01$  and the same radial resolution as in Sec. II A ( $n_r = 120$  radial grid points). We note that using a box size of  $[L_x/\rho_s, L_y/\rho_s] = [128, 128]$  results in energy diffusivities that are 5%–10% higher for the STD case with kinetic electrons.<sup>25</sup> However, we have found that increasing the radial resolution from  $n_r = 120$  to  $n_r = 160$  for the STD case results in a 5%–10% decrease in the energy diffusivities, thus offsetting the box size effect. The time-averaged diffusivities also exhibit some sensitivity to deviations of the perturbed temperatures and densities from the input values. In our simulations, we strived to limit this deviation to less than 5%. In any case, these deviations remain well within the rms deviations of the time-averaged diffusivities.

Linear stability analysis of the STD case with kinetic electrons indicates that all 16 toroidal modes propagate in the ion direction with a maximum linear growth rate and frequency of the ITG branch of  $[\gamma_{\max}, \omega] = [0.24, -0.33](c_s/a)$  at  $k_{\theta}\rho_s = 0.31$ . Figure 6 shows the time evolution of the turbulent ion heat [Fig. 6(a)], electron heat [Fig. 6(b)], and ion particle [Fig. 6(c)] diffusivities. The corresponding time-averaged diffusivities are  $\bar{\chi}_i/\chi_{GB} = 10.7 \pm 2.6$ ,  $\bar{\chi}_e/\chi_{GB} = 3.2 \pm 0.6$ , and  $\bar{D}/\chi_{GB} = -1.9 \pm 0.5$ . Figure 7 shows the normalized fractional diffusivities versus  $k_{\theta}\rho_s$ . Here, the area under the curves adds up to unity. While the peak in the growth rates is at  $k_{\theta}\rho_s = 0.31$ , the peak in the transport is near  $k_{\theta}\rho_s = 0.1$ . Compared with the adiabatic electron case, the ion heat diffusivity from the kinetic electron case has increased by a factor of approximately 3.5 with the addition of the

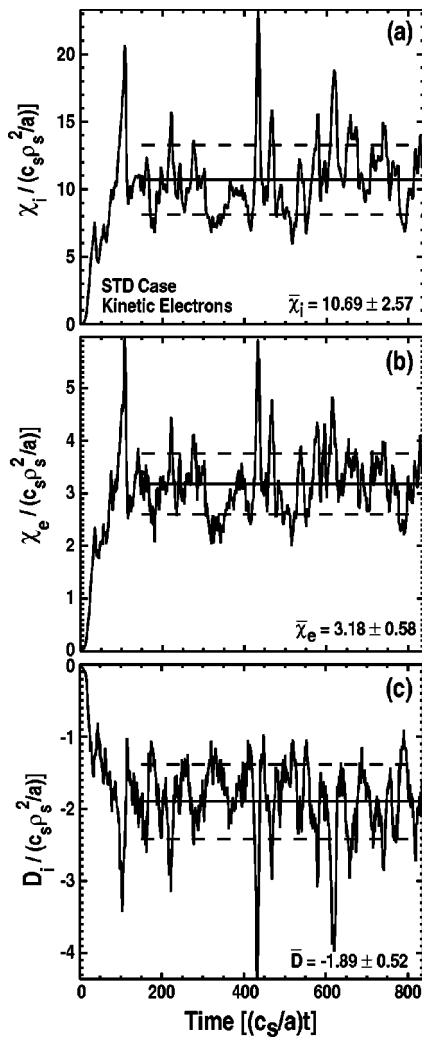


FIG. 6. Time evolution of the turbulent (a) ion heat, (b) electron heat, and (c) ion particle diffusivities for the standard case with kinetic electrons. The time-averaged values of the diffusivities are quoted in each panel.

trapped electron drive. The slow fall of in the spectrum of  $\chi_e$  suggests that larger values might be obtained with a more expensive higher-resolution ( $k_{\theta}\rho_s > 0.75$ ) simulation. However, a 32-mode simulation with  $k_{\theta}\rho_s \leq 1.55$  yields time-averaged ion and electron diffusivities that are only 7.5% higher. Here, we emphasize that  $\chi_i$  and  $\chi_e$  are flux surface-averaged energy flux diffusivities taking the form  $\chi_{e,i} = Q_{e,i} / (n_{e,i} T_{e,i} / L_{Te,i})$ , including convection, which in this case is inward. The particle diffusivity  $D = \Gamma / (n / L_n)$  is negative indicating a pinch or inward flux. Recent GYRO simulations by Estrada-Mila *et al.*,<sup>25</sup> which explain plasma pinches and impurity transport, show that the pinch is driven by electron temperature gradients.

### B. Standard case $E \times B$ shear scan

Rotational  $E \times B$  shear stabilizes the turbulence and reduces the heat, particle, and toroidal momentum transport. While the effect of  $E \times B$  shear on ITG transport has been widely investigated and published, the effect of  $E \times B$  shear in the presence of kinetic electrons has, until now, never been investigated. We find that for the standard case, the quench

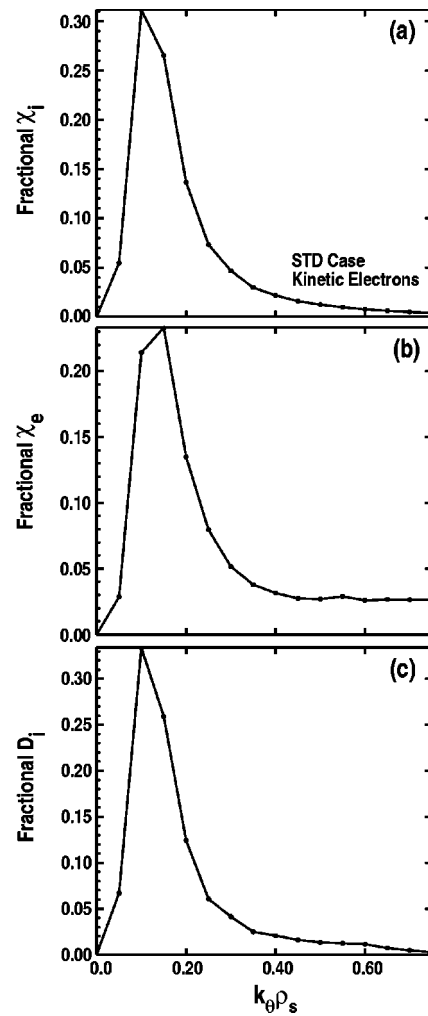


FIG. 7. Normalized fractional (a) ion heat, (b) electron heat, and (c) ion particle diffusivity vs  $k_{\theta}\rho_s$  time averaged for the standard case with kinetic electrons.

rule is still valid when kinetic electrons are included in the nonlinear gyrokinetic simulations. Figure 8 shows the ion (solid circles) and electron (hollow circles) heat diffusivity versus  $\gamma_E / \gamma_{\max(0)}$  with (dashed lines) and without (solid lines) the destabilizing effect of parallel velocity shear  $\gamma_p$ . The points are the GYRO results and the lines are curve fits. The quench point for the ion and electron transport is approximately  $\gamma_E / \gamma_{\max(0)} = 2.0$ , which is what we found for the adiabatic electron simulations (with  $\gamma_E$  restarts). Also, with a parallel velocity shear of  $\gamma_p = (Rq/r) \gamma_E = 12 \gamma_E$  included in the simulations, the transport is not quenched by any level of  $\gamma_E$ . Figure 9 shows the turbulent toroidal momentum diffusivity  $\bar{\chi}_{\phi} / \chi_{GB}$  and particle diffusivity  $\bar{D} / \chi_{GB}$  vs  $\gamma_E / \gamma_{\max(0)}$  for the case with  $\gamma_p = 12 \gamma_E$ . Notice that the particle pinch survives but is weakened as  $\gamma_E$  is increased.

In the absence of parallel velocity shear, the contributions to the total heat transport are reduced for every  $k_{\theta}\rho_s$  in the spectrum when  $E \times B$  shear is included. As  $\gamma_E$  is increased more and more of the low- $k$  modes are stabilized and the peak in the transport shifts to higher  $k_{\theta}\rho_s$ . Figure 10 shows the spectrum of the ion and electron heat diffusivities versus  $k_{\theta}\rho_s$  for  $\gamma_E = 0, 0.1, 0.2$ , and  $0.4$ . Here, the area under

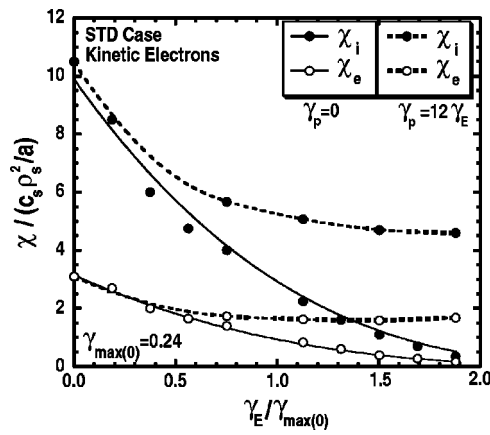


FIG. 8. Ion heat (solid circles) and electron heat (hollow circles) diffusivities vs  $\gamma_E/\gamma_{max(0)}$  with (dashed lines) and without (solid lines) the destabilizing effect of parallel velocity shear  $\gamma_p$ . The points are the GYRO results and the lines are curve fits.

the curves adds up to the time-averaged heat diffusivities. In comparison with  $\chi_i$ , the modes above  $k_{\theta}\rho_s=0.3$  contribute more to  $\chi_e$ . It appears that  $E \times B$  shear acts per mode, i.e.,  $\alpha_E \gamma_E > \gamma_k$  would quench a few  $k_{\theta}\rho_s$ , but the nonlinear transfer from unquenched higher  $k_{\theta}\rho_s$  modes replenishes the lower  $k_{\theta}\rho_s$  modes.

### C. Testing the $E \times B$ quench rule for electron modes

The validity of the  $E \times B$  quench rule has been established for long-wavelength turbulence with and without kinetic electrons in toroidal geometry. However, in the STD case, the low- $k$  part of the spectrum is dominated by ion-directed modes (up to approximately  $k_{\theta}\rho_s=0.7$ ). Thus, we are motivated to investigate how the turbulence responds to  $E \times B$  shear when the modes are in the electron direction. In this section, we present simulation results of  $E \times B$  shear scans for two cases where the low- $k$  unstable modes are either primarily or totally in the electron direction.

The first TEM case (TEM1) corresponds to the standard parameters with  $a/L_n=2$  and  $a/L_T=2$  ( $\eta=1$ ). Linear stability

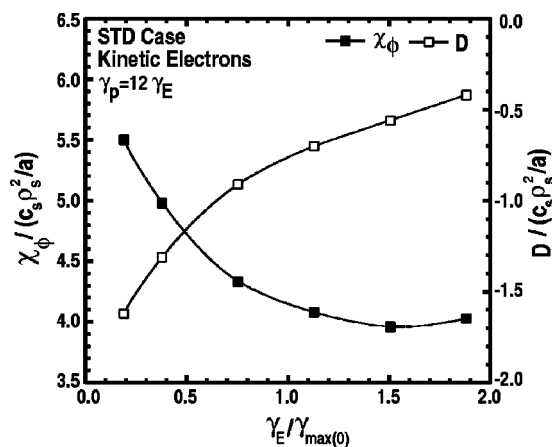


FIG. 9. Turbulent toroidal momentum (solid squares) and ion particle (hollow squares) diffusivities vs  $\gamma_E/\gamma_{max(0)}$  for the standard case with kinetic electrons and  $\gamma_p=12\gamma_E$ .

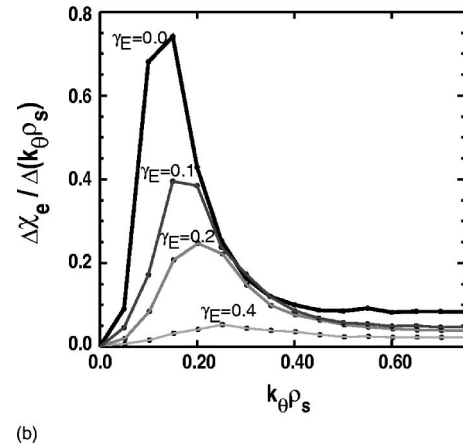
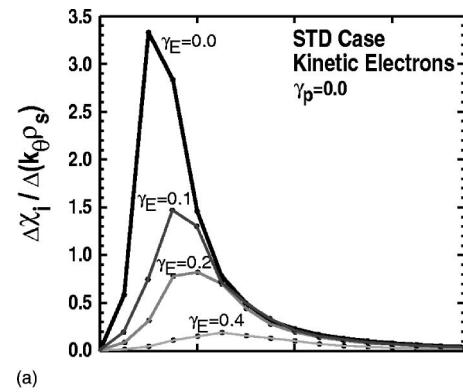


FIG. 10. Fractional absolute (a) ion and (b) electron heat diffusivities vs  $k_{\theta}\rho_s$  for  $\gamma_E=0, 0.1, 0.2$ , and  $0.4$ .

calculations for these parameters indicates that the mode frequencies are low (close to zero) and are either slightly negative (ion direction) or slightly positive (electron direction). Below  $k_{\theta}\rho_s=0.3$  the mode frequency is positive. The frequency is negative above  $k_{\theta}\rho_s=0.3$  due to finite Larmor radius effects. The maximum linear growth and frequency are  $[\gamma_{max(0)}, \omega]=[0.275, -0.014](c_s/a)$  at  $k_{\theta}\rho_s=0.29$ . Linear calculations with adiabatic electrons yields very small ITG growth rates with  $\gamma_{max(0)}=0.04$  at  $k_{\theta}\rho_s=0.25$ . Clearly, the TE drive dominates the pure ITG drive for these parameters. In fact, the TEM drive is so strong that  $\chi_e$  is comparable to  $\chi_i$  with  $\bar{\chi}_i/\chi_{GB}=11.0 \pm 2.2$ ,  $\bar{\chi}_e/\chi_{GB}=11.3 \pm 2.2$ , and  $\bar{D}_i/\chi_{GB}=4.0 \pm 0.8$ . The peak in the transport occurs near  $k_{\theta}\rho_s=0.10$ , which is surprisingly similar to the standard case. While the standard case showed a particle pinch,  $D_i$  is strongly outwardly diffusive for this TEM case. This case also differs from the standard case in that the modes above  $k_{\theta}\rho_s=0.3$  contribute little to  $\chi_e$ .

An  $E \times B$  shear scan around the TEM1 case shows that the quench point is higher than that found for the standard case. Here, the transport is quenched at approximately  $\gamma_E/\gamma_{max(0)}=2.5$ . Figure 11 shows the turbulent electron and ion heat diffusivity  $\bar{\chi}_{e,i}/\chi_{GB}$  along with the ion particle diffusivity  $\bar{D}/\chi_{GB}$  vs  $\gamma_E/\gamma_{max(0)}$ . Here, again we have set  $\gamma_p=0$ . The circles and squares correspond to the GYRO points and the lines represent linear fits. The GYRO points above



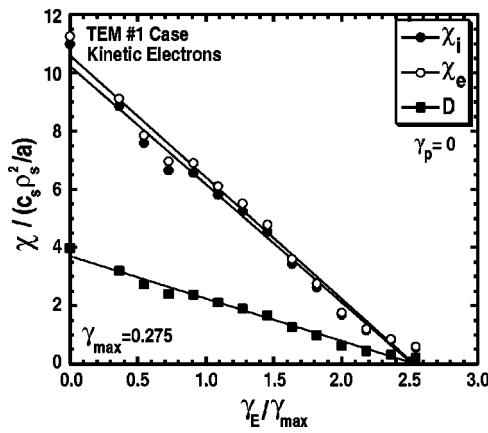


FIG. 11. Ion heat (solid circles), electron heat (hollow circles), and ion particle (squares) diffusivities vs  $\gamma_E/\gamma_{\max(0)}$  for the TEM1 case (standard parameters with  $a/L_n=2$  and  $a/L_T=2$ ).

$\gamma_E/\gamma_{\max(0)}=2$  exhibit some curvature suggesting that there may be a long tail in  $\chi$  vs  $\gamma_E/\gamma_{\max(0)}$  but such low transport levels are very difficult to resolve.

The second TEM case (TEM2) yields mode frequencies that are all clearly in the electron direction for  $k_{\theta}\rho_s \leq 0.65$ . The parameters are the same as the standard case but with  $a/L_n=3$  and  $a/L_T=1$  ( $\eta=1/3$ ). For this case, the maximum linear growth and frequency are  $[\gamma_{\max(0)}, \omega] = [0.43, 0.029](c_s/a)$  at  $k_{\theta}\rho_s=0.51$ . The simulations were performed with 16 modes and a toroidal spacing of  $\Delta n=8$  at  $\rho_s=0.0025$  to give a maximum  $k_{\theta}\rho_s$  of 1.2. The number of radial grid points was increased from the standard case value of 120 to 160 in order to properly resolve the finer scale higher- $k$  modes. In the absence of  $E \times B$  shear, the transport levels are large with  $\bar{\chi}_i/\chi_{GB}=20.5 \pm 4.8$ ,  $\bar{\chi}_e/\chi_{GB}=23.9 \pm 5.9$ , and  $\bar{D}_i/\chi_{GB}=4.8 \pm 1.2$ . A complimentary simulation with 32 modes and a maximum  $k_{\theta}\rho_s$  of 1.55 yields somewhat higher transport levels with  $\bar{\chi}_i/\chi_{GB}=23.9 \pm 3.7$ ,  $\bar{\chi}_e/\chi_{GB}=27.7 \pm 4.5$ , and  $\bar{D}_i/\chi_{GB}=5.6 \pm 0.9$ . Figure 12(a) shows the time evolution of the turbulent ion heat (thick lines) and electron heat (thin lines) for the 32-mode TEM2 case with  $\gamma_E=0$ . The normalized fractional ion heat diffusivity versus  $k_{\theta}\rho_s$  is shown in Fig. 12(b). Both the electron heat and ion particle fractional diffusivity curves are nearly identical to the ion heat diffusivity curve. Beyond  $k_{\theta}\rho_s=0.6$ , very little is contributed to the transport.

An  $E \times B$  shear scan around the TEM2 case shows that the quench point is at approximately  $\gamma_E/\gamma_{\max(0)}=2.1$ . This is somewhat lower than the intermediate TEM case (TEM1) but amazingly similar to the results for the standard case where all the modes are in the ion direction. Figure 13 shows the turbulent electron and ion heat diffusivity  $\chi_{e,i}/c_s \rho_s^2/a$  along with the ion particle diffusivity  $D_i/c_s \rho_s^2/a$  vs  $\gamma_E/\gamma_{\max(0)}$ . The circles (solid and hollow) denote the ion and electron heat diffusivities and the squares correspond to the particle diffusivity. The lines represent linear fits to the GYRO points. The simulations used 16 toroidal modes. Several 32-mode cases compliment the scan and have a maxi-

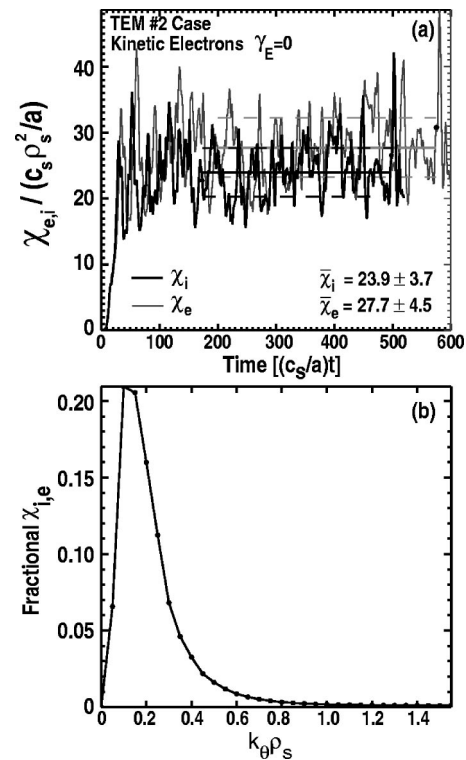


FIG. 12. (a) Time evolution of the turbulent ion (thick line) and electron (thin line) heat diffusivities for the TEM2 case (standard parameters with  $a/L_n=3$  and  $a/L_T=1$ ) and (b) normalized fractional ion heat diffusivity vs  $k_{\theta}\rho_s$ .

mum  $k_{\theta}\rho_s$  of 1.55. Higher  $k_{\theta}\rho_s$  modes contribute little to the transport, so the 32-mode simulations yield approximately the same diffusivities as the 16-mode simulations.

#### IV. CONCLUSIONS

We have investigated the effect of  $E \times B$  flow shear in nonlinear gyrokinetic simulations with and without kinetic electrons. Case studies have been performed using the GYRO code<sup>23</sup> around a standard test case with  $R/a=3.0$ ,  $r/a=0.5$ ,  $q=2$ ,  $\hat{s}=1.0$ ,  $\beta=0$ ,  $\alpha=0$ ,  $a/L_n=1.0$ ,  $a/L_T=3.0$ ,  $\nu_{e,i}=0.0c_s/a$ , and  $T_i/T_e=1.0$ . We find that the  $E \times B$  shear

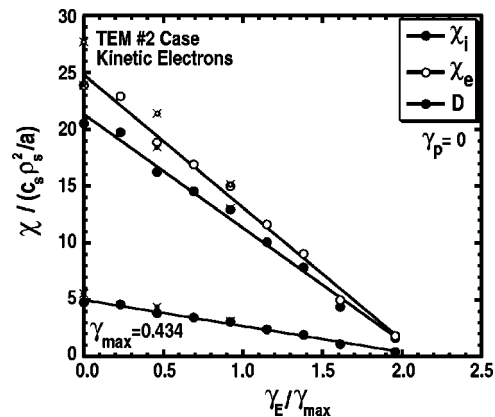


FIG. 13. Ion heat (solid circles), electron heat (hollow circles), and ion particle (squares) diffusivities vs  $\gamma_E/\gamma_{\max(0)}$  for the TEM2 case. The 32-mode simulations are indicated with circles having crosses.

quench rule, originally deduced from adiabatic electron ITG simulations, also applies in the presence of kinetic electrons for long-wavelength modes. In the absence of parallel velocity shear, we find that the quench point is fairly robust at  $\gamma_E/\gamma_{\max}=2\pm 0.5$  ( $\alpha_E=0.5$ ) for both the adiabatic and kinetic electron cases examined. This is twice the value previously found in nonlinear gyrofluid simulations where the quench point was approximately  $\gamma_E/\gamma_{\max}=1\pm 0.3$ . In kinetic electron simulations of peaked density cases, where the unstable modes are primarily in the electron direction, the  $E\times B$  shear quench point occurs at somewhat higher values in the range of  $\gamma_E/\gamma_{\max(0)}=2.1-2.5$ .

In both adiabatic and kinetic electron scans in  $\gamma_E$  where the destabilizing effect of parallel velocity shear is included, the transport may not be quenched by  $E\times B$  shear for large values of the safety factor. For the standard case assuming purely toroidal rotation, we find that the Kelvin–Helmholtz drive increases  $\gamma_{\max}$  faster than  $\gamma_E$  increases and only a modest reduction in the transport from  $E\times B$  shear stabilization is achieved. Here,  $\gamma_p=(Rq/r)\gamma_E=12\gamma_E$  with  $R/a=3$ ,  $r/a=0.5$ , and  $q=2$ . This trend holds for high  $Rq/r$ , thus low- $q$  is advantageous for maximizing  $\gamma_E$  stabilization.

In the proximity of the quench point, adiabatic electron simulations have revealed that two different equilibrium states can be found at a critical  $E\times B$  shear rate,  $\gamma_E^{\text{crit}}$ , depending upon how the  $\gamma_E$  is applied. Simulations initiated with  $\gamma_E^{\text{crit}}$  yield zero transport levels. However, if the simulation is restarted with from a state where  $\gamma_E=0$ , then increasing  $\gamma_E$  to  $\gamma_E^{\text{crit}}$ , then the turbulence levels are not quenched and are merely suppressed to some finite level. We have not observed this same phenomenon in kinetic electron simulations.

It appears that  $E\times B$  shear has more effect on more weakly driven modes in that modes satisfying  $\alpha_E\gamma_E>\gamma_k$  tend to be quenched [as built into the GLF23 (Ref. 8) mixing length rule], but the nonlinear transfer from unquenched higher  $k_{\theta\rho_s}$  modes replenishes the lower  $k_{\theta\rho_s}$  modes. As the level of  $\gamma_E$  is increased there is an upshift in the spectrum of the transport with an increasingly larger relative contribution to the fluxes from higher  $k_{\theta\rho_s}$  unstable modes. That all channels (ion and electron energy flux and particle flux) appear to quench in the same linear fashion ( $1-\alpha_E\gamma_E/\gamma_{\max}$ ) suggests that quasilinear formulas can describe the fluxes quite well.

The robustness of the quench point and the above features strongly suggests the existence of a linear method that could describe  $E\times B$  shear stabilization. A linear method would be very useful in quantifying the weak parametric dependence of the quench point on parameters such as the magnetic shear, safety factor, and elongation. It is well known that linear eigenmodes do not exist for  $E\times B$  shear in toroidal geometry.<sup>6</sup>  $E\times B$  shear causes Floquet modes which rotate in the poloidal angle from bad to good curvatures. The instantaneous growth rate of the Floquet modes oscillates

with a period of  $2\pi\hat{s}/\gamma_E$  between positive and negative values. Future work is needed to identify the quench point with some average null linear growth rate.

## ACKNOWLEDGMENTS

We thank Dr. M. Fahey of Oak Ridge National Laboratory (ORNL) for technical support. The simulations were made possible through generous allotments of computer time on the IBM SP Power4 (Cheetah) at ORNL and on the IBM SP Power3 (Seaborg) at NERSC.

This work was supported by the U.S. Department of Energy under Grant Nos. DE-FG03-95ER54309 and DE-FG03-92ER54141.

- <sup>1</sup>H. Biglari, P. H. Diamond, and P. Terry, *Phys. Fluids B* **2**, 1 (1990).
- <sup>2</sup>K. C. Shaing, J. E. C. Crume, and W. Houlberg, *Phys. Fluids B* **2**, 1492 (1990).
- <sup>3</sup>Y. Z. Zhang and S. Mahajan, *Phys. Fluids B* **2**, 1385 (1992).
- <sup>4</sup>R. E. Waltz, G. D. Kerbel, and J. Milovich, *Phys. Plasmas* **1**, 2229 (1994).
- <sup>5</sup>R. E. Waltz, G. D. Kerbel, J. Milovich, and G. W. Hammett, *Phys. Plasmas* **2**, 2408 (1995).
- <sup>6</sup>R. E. Waltz, R. L. Dewar, and X. Garbet, *Phys. Plasmas* **5**, 1784 (1998).
- <sup>7</sup>R. E. Waltz, G. M. Staebler, G. W. Hammett, and J. A. Konings, in *Controlled Fusion and Plasma Physics*, Proceedings of the Sixteenth IAEA Fusion Energy Conference, Montréal, 1996 (International Atomic Energy Agency, Vienna, in press), paper IAEA-CN-64/D1-6.
- <sup>8</sup>R. E. Waltz, G. M. Staebler, W. Dorland, G. W. Hammett, M. Kotschenreuther, and J. A. Konings, *Phys. Plasmas* **4**, 2482 (1997).
- <sup>9</sup>M. Kotschenreuther, W. Dorland, M. A. Beer, and G. W. Hammett, *Phys. Plasmas* **2**, 2381 (1995).
- <sup>10</sup>R. E. Waltz, J. M. Candy, and M. N. Rosenbluth, *Phys. Plasmas* **9**, 1938 (2002).
- <sup>11</sup>A. M. Dimits, B. I. Cohen, W. M. Nevins, and D. E. Shumaker, in *Controlled Fusion and Plasma Physics*, Proceedings of the Eighteenth IAEA Fusion Energy Conference, Sorrento, 2000 (International Atomic Energy Agency, Vienna), paper THP1-03.
- <sup>12</sup>R. E. Waltz and R. L. Miller, *Phys. Plasmas* **6**, 4265 (1999).
- <sup>13</sup>J. E. Kinsey, G. M. Staebler, and R. E. Waltz, *Phys. Plasmas* **9**, 1676 (2002).
- <sup>14</sup>C. M. Greenfield, D. P. Schissel, B. W. Stallard, E. A. Lazarus, G. A. Navratil, T. A. Casper, J. C. DeBoo, E. J. Doyle, R. J. Fonck, and C. B. Forest, *Phys. Plasmas* **4**, 1596 (1997).
- <sup>15</sup>M. Beer, G. W. Hammett, G. Rewoldt *et al.*, *Phys. Plasmas* **4**, 1792 (1997).
- <sup>16</sup>E. J. Synakowski, S. H. Batha, M. A. Beer *et al.*, *Phys. Plasmas* **4**, 1736 (1997).
- <sup>17</sup>K. H. Burrell, M. E. Austin, C. M. Greenfield, L. L. Lao, B. W. Rice, G. M. Staebler, and B. W. Stallard, *Plasma Phys. Controlled Fusion* **40**, 1585 (1998).
- <sup>18</sup>B. W. Stallard, C. M. Greenfield, G. M. Staebler, C. L. Rettig, M. S. Chu, M. E. Austin, D. R. Baker, L. R. Baylor, K. H. Burrell, J. C. DeBoo, J. S. deGrassie, E. J. Doyle, J. Lohr, G. R. McKee, R. L. Miller, W. A. Peebles, C. C. Petty, R. I. Pinsker, B. W. Rice, T. L. Rhodes, R. E. Waltz, L. Zeng, and the DIII-D Team, *Phys. Plasmas* **6**, 1978 (1999).
- <sup>19</sup>R. V. Budny, R. Andre, A. Becoulet, C. D. Challis, G. Conway, W. Dorland, D. Ernst, T. Hahm, T. Hender, D. McCune, G. Rewoldt, S. E. Sharapov, and contributors to the EFDA-JET work programme, *Plasma Phys. Controlled Fusion* **44**, 1215 (2002).
- <sup>20</sup>R. R. Dominguez and G. M. Staebler, *Phys. Fluids B* **5**, 3876 (1993).
- <sup>21</sup>F. Jenko, W. Dorland, M. Kotschenreuther, and B. N. Rodgers, *Phys. Plasmas* **7**, 1904 (2000).
- <sup>22</sup>F. Jenko and W. Dorland, *Phys. Rev. Lett.* **89**, 225001 (2002).
- <sup>23</sup>J. Candy and R. E. Waltz, *Phys. Rev. Lett.* **91**, 45001 (2003).
- <sup>24</sup>J. W. Connor, R. J. Hastie, and J. B. Taylor, *Phys. Rev. Lett.* **40**, 396 (1978).
- <sup>25</sup>C. Estrada-Mila, R. E. Waltz, and J. M. Candy, *Phys. Plasmas* **12**, 022305 (2005).